Effective Model Analysis of Intrinsic Spin Hall Effect with Magnetism in the Stacked Kagome Weyl Semimetal $Co_3Sn_2S_2$

Akihiro Ozawa,[1,*,§] Koji Kobayashi,[2,†,¶] and Kentaro Nomura[2,‡]

[1] *Institute for Materials Research, Tohoku University, Sendai 980-8577, Japan*
[2] *Department of Physics, Kyushu University, Fukuoka 819-0395, Japan*

(Received 25 May 2023; revised 21 November 2023; accepted 22 December 2023; published 22 January 2024)

We theoretically study the spin Hall effect in a simple tight-binding model of the stacked kagome Weyl semimetal $Co_3Sn_2S_2$ with ferromagnetic ordering. We focus on the two types of spin Hall current: one flowing in the in-plane direction with respect to the kagome lattice (in-plane spin Hall current), and the other flowing in the stacking direction (out-of-plane spin Hall current). We show that the spin Hall conductivities for those spin currents drastically change depending on the direction of the magnetic moment. In particular, the out-of-plane spin Hall current may induce surface spin accumulations, which are useful for magnetization switching via spin-orbit torque.

DOI: 10.1103/PhysRevApplied.21.014041

I. INTRODUCTION

The generation and control of spin current, that is, the flow of spin angular momentum, are important objectives in spintronics. The spin Hall effect (SHE) [1–3] is one of the fundamental phenomena for generating spin current; the spin current is driven transversely to an applied electric field. Spin-orbit coupling (SOC) plays a significant role in obtaining the spin-dependent electron motion and thus the SHE. The highly efficient SHE-based manipulation of magnetization, such as spin-orbit torque (SOT) [4–9], has recently been studied. Conventionally, nonmagnetic materials with a strong SOC, such as Pt [10] and Ta [8], had been examined as a spin Hall current generator. Meanwhile, in such a system, the direction of the accumulated spin at the interface is constrained to be perpendicular to both the direction of the flow of spin current and the applied electric field [1,3].

In addition to nonmagnetic materials, recent studies explore the possibility of magnetic materials as spin Hall systems [11–18]. In particular, some magnetic systems exhibit a peculiar SHE where the direction of the accumulated spin is parallel to that of flow of spin current, depending on the magnetic configurations, such as antiferromagnetic ordering [18–20]. Finding spin Hall systems without restrictions on the direction of induced spin accumulation may help us design functional spintronic devices.

Recently, from the viewpoint of spintronic functionalities, magnetic Weyl semimetals have been studied [21–26]. Originating from the Berry curvature generated by the band crossing points (Weyl points) [27,28], distinctive electromagnetic responses, such as the intrinsic anomalous Hall effect (AHE) [28], occur. ABC-stacked kagome lattice ferromagnet $Co_3Sn_2S_2$ is a promising candidate for a magnetic Weyl semimetal [29–32]. The giant AHE arises because the Weyl points are very close to the Fermi level. Additionally, the giant anomalous Hall angle is realized due to the small longitudinal conductivity, i.e., the small Fermi surfaces [29]. Other characteristic responses, such as the anomalous Nernst effect [33] and the magneto-optical Kerr effect [34], are also studied. According to the above features, we expect $Co_3Sn_2S_2$ might be useful for the efficient and functional manipulations of the spin current for the following reasons. First, the fully polarized current is realized because of the half-metallicity [29,35]. Thus the giant anomalous Hall angle implies a highly efficient SHE. Second, owing to SOC, the band topology and AHE depend on the magnetic configurations [36–38]. Similarly, the characteristic relations between the SHE and the direction of the magnetic moments are expected. As a matter of fact, a recent experiment reported an SOT with high spin-change conversion efficiency in the ferromagnetic phase of $Co_3Sn_2S_2$ [39]. However, the theoretical understanding of the role of magnetic orderings for spin transport in this system is still limited.

*akihiroozawa@issp.u-tokyo.ac.jp
†k-koji@sophia.ac.jp
‡nomura.kentaro@phys.kyushu-u.ac.jp
§Present address: Institute for Solid State Physics, University of Tokyo, Kashiwa 277-8581, Japan.
¶Present address: Physics Division, Sophia University, Chiyoda-ku, Tokyo 102-8554, Japan.

In this paper, we theoretically investigate the SHE and AHE in an effective tight-binding model [40] of the magnetic Weyl semimetal $Co_3Sn_2S_2$ with ferromagnetic ordering. First, we recall that this model can describe the Dirac semimetal state and the SHE in a nonmagnetic state. Then we show that spin Hall conductivities (SHCs) drastically change depending on the direction of the magnetic moment. In particular, the out-of-plane SHE is enhanced by tilting the magnetic moment from the z axis, in the presence of a certain SOC. Lastly, the potential of this system as a spin-current generator for magnetization switching is discussed.

II. TIGHT-BINDING MODEL

First, we explain the minimal tight-binding model of the magnetic Weyl semimetal $Co_3Sn_2S_2$ introduced in our previous study Ref. [40]. This model describes the three pairs of Weyl points by using the d orbital of Co and the p orbital of interlayer Sn, as shown in the following section. Figure 1(a) shows the crystal structure of $Co_3Sn_2S_2$. The kagome lattice consists of Co, which is responsible for magnetism. Sn atoms are located at the center of these hexagons of the kagome lattice. Triangular lattice layers formed by one Sn and two S are sandwiched by the kagome layers. To distinguish two different Sn, we use the notation Sn1 and Sn2 for interlayer Sn and intralayer Sn, respectively. In our effective model, one d orbital from Co forming the kagome layers (red) and one p orbital from interlayer Sn1 (blue) are extracted. We neglect the rest of the orbitals from another Sn2 (cyan) and S (green) for simplicity. The effect of those neglected sites is substantially incorporated into the model as an electric field yielding an SOC, as discussed in what follows. Therefore the unit cell consists of the $(3+1)$ sublattices. The primitive translational vectors are defined as $\mathbf{a}_1 = (a/\sqrt{3}, 0, c/3)$, $\mathbf{a}_2 = (-a/2\sqrt{3}, a/2, c/3)$, $\mathbf{a}_3 = (-a/2\sqrt{3}, -a/2, c/3)$. Here, a and c are lattice parameters of the conventional unit cell, given as $a = 5.37$ Å and $c = 13.18$ Å [29], respectively.

The total Hamiltonian of this model is given by

$$H_0 = H_{hop} + H_{soc} + H_{exc}. \tag{1}$$

Here, H_{hop} is the spin-independent hopping term, H_{soc} is the SOC term, and H_{exc} is the exchange coupling term between electron spins and the magnetic moment. Here H_{hop} is given by

$$H_{hop} = -\sum_{ijs} t_{ij}\, d^\dagger_{is} d_{js} + t_{dp} \sum_{\langle ij \rangle s} (d^\dagger_{is} p_{js} + p^\dagger_{is} d_{js}) + \epsilon_p \sum_{is} p^\dagger_{is} p_{is}, \tag{2}$$

where d_{is} and p_{is} are the annihilation operators of the Co d and Sn p orbitals, respectively. The index s is for the spin, and i for the site. The term t_{ij} includes the first- and second-nearest-neighbor hopping, t_1 and t_2, in the kagome layer, interkagome layer hopping t_z. The summation for $\langle ij \rangle$ is taken over the nearest-neighbor hopping between the Co and Sn sites. t_{dp} represents the dp hybridization between the Co d and Sn p orbitals. The lattice vectors for the intralayer nearest-neighboring are calculated by $\mathbf{b}_{AB} = (\mathbf{a}_2 - \mathbf{a}_1)/2$, $\mathbf{b}_{BC} = (\mathbf{a}_3 - \mathbf{a}_2)/2$, and $\mathbf{b}_{CA} = (\mathbf{a}_1 - \mathbf{a}_3)/2$. In the same manner, the lattice vectors for intralayer second-nearest-neighboring are calculated by $\mathbf{d}_{AB} = (\mathbf{b}_3 - \mathbf{b}_2)/2$, $\mathbf{d}_{BC} = (\mathbf{b}_3 - \mathbf{b}_2)/2$, and $\mathbf{d}_{CA} = (\mathbf{b}_1 - \mathbf{b}_3)/2$. The lattice vectors for the interlayer nearest-neighboring are calculated by $\mathbf{c}_{AB} = (\mathbf{a}_1 - \mathbf{a}_2)/2$, $\mathbf{c}_{BC} = (\mathbf{a}_2 - \mathbf{a}_3)/2$, and $\mathbf{c}_{CA} = (\mathbf{a}_3 - \mathbf{a}_1)/2$. Here, A, B and C are the sublattice indices [40].

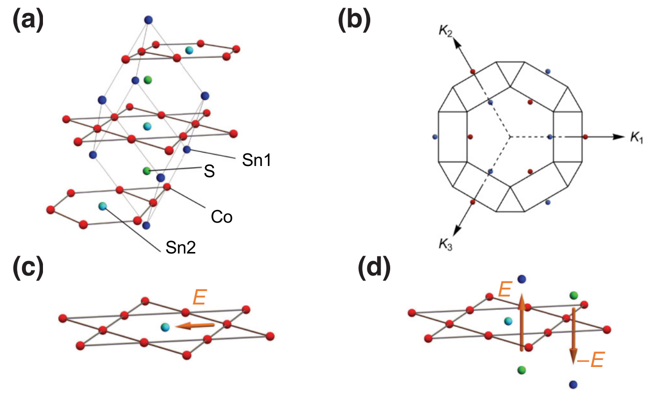

FIG. 1. (a) Crystal structure of $Co_3Sn_2S_2$. (b) The Weyl points configuration computed by our model. (c) Electric field generated by a Co nucleus (red) and Sn nucleus (cyan) at the center of the hexagon in the kagome layer, giving rise to intralayer-kagome type SOC. (d) Electric field generated by a Sn nucleus (blue) and S nucleus (green) in between the kagome layers, giving rise to the staggered Rashba type SOC.

The SOC term is given by $H_{soc} = H_{KM} + H_{sR}$, where

$$H_{KM} = -\mathrm{i}t_{KM} \sum_{\langle\langle ij \rangle\rangle ss'} \nu_{ij} \cdot d^\dagger_{is} \sigma^z_{ss'} d_{js'}, \tag{3}$$

$$H_{sR} = -\mathrm{i}t_{sR} \sum_{\langle ij \rangle ss'} \boldsymbol{\lambda}_{ij} \cdot d^\dagger_{is} \boldsymbol{\sigma}_{ss'} d_{js'}. \tag{4}$$

Here, H_{KM} describes the intrakagome-layer Kane-Mele type SOC [41,42] with strength t_{KM}. $\boldsymbol{\sigma}$ is the vector of Pauli matrices, corresponding to the electron spin. The sign is $\nu_{ij} = +1(-1)$ when the electron hops counterclockwise (clockwise) to reach the second-nearest-neighbor site on the kagome plane. The summation $\langle\langle ij \rangle\rangle$ is taken for intralayer second-nearest-neighbor sites. As shown in Fig. 1(c), this SOC originates from the potential of Sn at the center of hexagons of the kagome lattice. Then we explain the staggered Rashba type SOC H_{sR} as introduced in [43]. In $Co_3Sn_2S_2$, this SOC originates from the local inversion symmetry breaking of the Sn and S sites, as discussed in the following. As shown in Fig. 1(d), when we focus on one of the triangular plaquettes of the kagome lattice, Sn is located on the top while S is located at the bottom. Its nearest-neighboring plaquettes have the reverse configuration. Therefore, a perpendicular electric field penetrates each triangular plaquette in a staggered pattern. We use $\boldsymbol{\lambda}_{ij}$ to denote the effective magnetic field vector from the electric field when the electron hops from site j to site i. $\boldsymbol{\lambda}_{AB} = (\frac{1}{2}, \frac{\sqrt{3}}{2}, 0)$, $\boldsymbol{\lambda}_{BC} = (-1, 0, 0)$, $\boldsymbol{\lambda}_{CA} = (\frac{1}{2}, -\frac{\sqrt{3}}{2}, 0)$. The summation $\langle ij \rangle$ is taken for intralayer nearest-neighbor sites. This staggered Rashba type SOC has a significant role in obtaining the finite out-of-plane AHE and SHE, as discussed later.

The exchange coupling between the itinerant electron's spin and magnetic moments on the kagome lattice is given by

$$H_{exc} = -J \sum_{iss'} \mathbf{m}_i \cdot (d^{\dagger}_{is} \boldsymbol{\sigma}_{ss'} d_{is'} + p^{\dagger}_{is} \boldsymbol{\sigma}_{ss'} p_{is'}). \qquad (5)$$

Here, J is the exchange coupling constant and $\mathbf{m}_i$ is the vector of magnetic moment. We note that $\mathbf{m}_i$ should be calculated self-consistently with the Coulomb interaction [44]. We set the same value of exchange coupling on Co and Sn site for simplicity. In the following, we set t_1 as a unit of energy, $t_2 = 0.6t_1$, $t_{dp} = 1.8t_1$, $t_z = -1.0t_1$, $\epsilon_p = -7.2t_1$, $t_{KM} = -0.1t_1$, $t_{sR} = 0.1t_1$, and $J = 1.2t_1$. These parameters are also chosen to fit the band structure to the result obtained by first-principles calculations [29,45]. In the following, we study the SHC and anomalous Hall conductivity (AHC) based on this tight-binding model.

III. FERROMAGNETIC WEYL SEMIMETAL STATE AND NONMAGNETIC DIRAC STATE

To keep this paper self-contained, here we recall the ferromagnetic Weyl state and the paramagnetic Dirac state in the model as discussed in [46]. In Fig. 2(a), the energy spectrum of the spin-splitting Weyl state is schematically shown. The band structure in the ferromagnetic state is shown in Fig. 2(c). The red and blue lines are the spin-up band and spin-down band, respectively. We should note that the spin-up band and spin-down band cannot be identified when the staggered Rashba type SOC is considered. However, for visibility of the spin-polarized electronic structure, here we consider only the Kane-Mele type SOC, which preserves spin s_z. In the following sections, we discuss the role of staggered Rashba type SOC for the SHE. We do not show the lowest and second lowest bands, because they are energetically far from E_F. The Weyl pairs near E_F are formed with spin-up (red) bands, indicated by the red box. The Weyl points configuration seen from the k_z axis, computed by our model, is shown in Fig. 1(b). The threefold symmetry with respect to the k_z axis and the number of the Weyl points in the Brillouin zone are consistent with first-principles calculations [40]. Figure 2(d) is the density of states (DOS) as a function of the energy, computed with $\mathbf{m} = (0, 0, 1)$. We use $t_1 = 0.15$ eV as a unit of energy. $E = 0$ eV is set as E_F obtained by the electron number per unit cell $n_e = 3$, corresponding to E_F of nondoped $Co_3Sn_2S_2$ [40,44]. The DOS shows a local minimum near E_F, corresponding to the energy of the Weyl points. In the Weyl semimetal state the AHE occurs, as schematically shown in Fig. 2(b). Figure 2(e) shows $\sigma^{\mathrm{AHE}}_{yx}$ as a function of energy. Here, the AHC is calculated by the Kubo formula [47] as

$$\sigma^{\mathrm{AHE}}_{yx} = e^2 \hbar \sum_{n \neq m} \mathrm{Im} \int_{\mathrm{BZ}} \frac{d^3k}{(2\pi)^3} \frac{f(E_{n\mathbf{k}}) - f(E_{m\mathbf{k}})}{(E_{n\mathbf{k}} - E_{m\mathbf{k}})^2} \times \langle n\mathbf{k} | \hat{v}_y | m\mathbf{k} \rangle \langle m\mathbf{k} | \hat{v}_x | n\mathbf{k} \rangle . \qquad (6)$$

Here, $\hat{v}_i = (1/\hbar)(\partial H(\mathbf{k})/\partial k_i)$ $(i = x, y)$ is the velocity operator. f is the Fermi-Dirac distribution function with $k_B T = 0.01t_1$. The AHC is maximized near E_F, originating from the Berry curvature generated by the Weyl points. As we discussed in our previous study [40], the value of approximately 1000 [S/cm] is very close to the result obtained by first-principles calculations and experiment [29]. We note that, in addition to the electronic structure, our model also quantitatively explains the doping effect for magnetic orderings, as discussed in Ref. [44]. The perpendicular ferromagnetic ordering in the nondoped regime and suppression of the magnetism in the hole-doped regime obtained by the self-consistent method also agree with the first-principles calculations [45]. Therefore, our model is reasonable for describing the electronic state including the Weyl points near the Fermi level in $Co_3Sn_2S_2$.

Next, we explain the paramagnetic Dirac semimetal state and the SHE [46]. In Fig. 2(f), the energy spectrum of the paramagnetic Dirac state is schematically shown. Figures 2(h) and 2(i) show the spin degenerate band structure and DOS as a function of the energy, using the parameter $\mathbf{m} = (0, 0, 0)$. We emphasize that the energy of the Dirac points is located at $E \sim 0.1$ eV, deviating from E_F. In the Dirac semimetal state the SHE occurs, as schematically shown in Fig. 2(g). We focus on the spin current driven by an electric field pointing in the x-direction. The SHCs can be calculated as

$$\sigma^{s_\mu}_{\nu x} = \hbar \sum_{n \neq m} \mathrm{Im} \int_{\mathrm{BZ}} \frac{d^3k}{(2\pi)^3} \frac{f(E_{n\mathbf{k}}) - f(E_{m\mathbf{k}})}{(E_{n\mathbf{k}} - E_{m\mathbf{k}})^2} \times \langle n\mathbf{k} | \hat{j}^{\mu}_{\nu} | m\mathbf{k} \rangle \langle m\mathbf{k} | (-e\hat{v}_x) | n\mathbf{k} \rangle , \qquad (7)$$

where $\hat{j}^{\mu}_{\nu}$ is a spin-current operator with a spin polarization μ and spatial direction ν, given by $\hat{j}^{\mu}_{\nu} = \frac{1}{2}\{(\hbar/2)\sigma_\mu, \hat{v}_\nu\}$

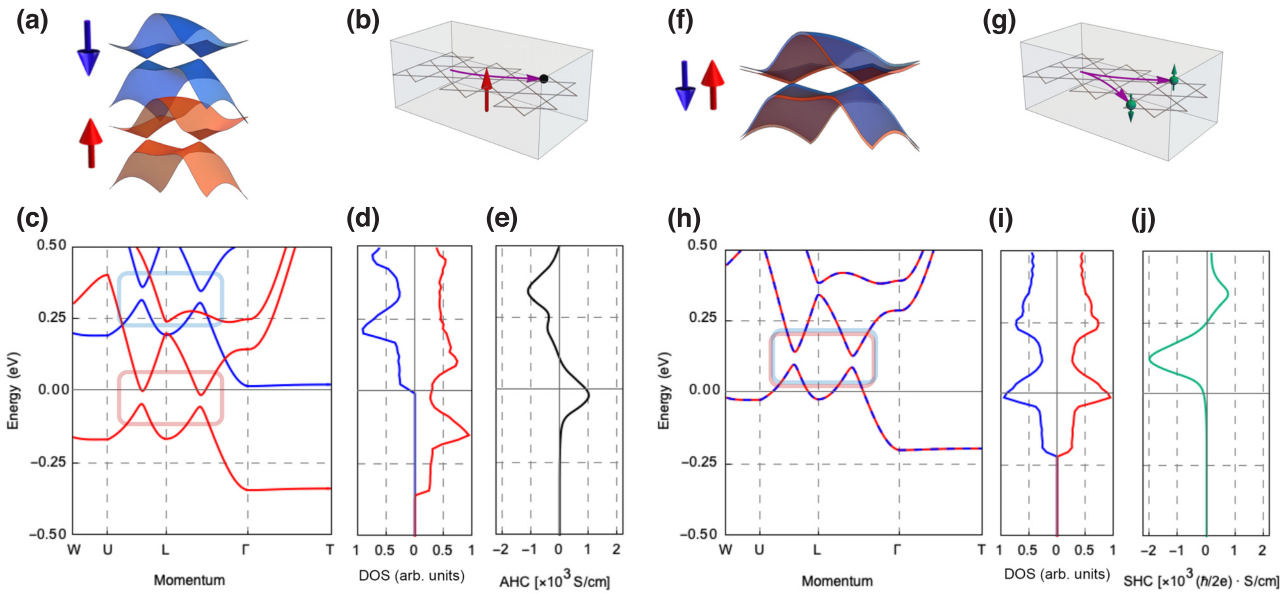

FIG. 2. For the magnetic Weyl semimetal state in this model, (a) schematic representation of the band structure and (b) the anomalous Hall effect, (c) the band structure along the high-symmetry line, (d) the density of states, and (e) the anomalous Hall conductivity. For the Dirac semimetal state, (f) schematic representation of the band structure and (g) the spin Hall effect, (h) the band structure along the high-symmetry line, (i) the density of states, and (j) the spin Hall conductivity. The Fermi level is calculated with a constant electron number $n_e = 3$ per unit cell.

[3]. We neglect an extrinsic contribution from impurities for simplicity. Figure 2(j) shows $\sigma_{yx}^{s_\mu}$ as a function of the energy. Near the energy of the Dirac points, corresponding to the minimum of the DOS, $\sigma_{yx}^{s_\mu}$ is maximized. To obtain the maximized SHC originating from the Dirac points, an appropriate tuning of E_F is required [46].

IV. IN-PLANE SPIN/ANOMALOUS HALL EFFECT

In the previous section, we recalled that our model describes the SHE and AHE originating from the nonmagnetic Dirac state and ferromagnetic Weyl state, respectively. As we mentioned in Sec. I, a recent experiment reported an SOT with high spin-charge conversion efficiency in a device based on $Co_3Sn_2S_2$ and CoFeB film [39]. In the device, an in-plane magnetized CoFeB is attached to the top surface of $Co_3Sn_2S_2$. In addition, it was predicted that the $Co_3Sn_2S_2$ in this device possesses an in-plane component of the magnetization near the interface [39], although the single system has a strong perpendicular magnetic anisotropy [48]. Motivated by these experimental results, we study the relation between the SHCs and the direction of the magnetization. In this section, we study the in-plane SHE (AHE), where the spin (anomalous) Hall current $j_y^{s_\mu}$ (j_y^{AHE}) is induced by an electric field E_x, as schematically shown in Figs. 3(a)–3(d). The in-plane SHCs and AHC are denoted by $\sigma_{yx}^{s_\mu}$ and $\sigma_{yx}^{\mathrm{AHE}}$, respectively. Then we introduce the magnetic moments in different directions, which are characterized by the parameter $\mathbf{m}_i$ in the exchange coupling term Eq. (5). For simplicity, we focus on the uniform tilting of the magnetization in the bulk model and introduce the tilting angles as tunable parameters. We use uniform magnetization with three tilting angles in (e) the x-z plane (α), (h) the y-z plane (β), and (k) the x-y plane (γ), as shown in Fig. 3. These magnetic configurations are given by (e) $\mathbf{m}_A = \mathbf{m}_B = \mathbf{m}_C = m(\sin\alpha, 0, \cos\alpha)$, (h) $\mathbf{m}_A = \mathbf{m}_B = \mathbf{m}_C = m(0, \sin\beta, \cos\beta)$, (k) $\mathbf{m}_A = \mathbf{m}_B = \mathbf{m}_C = m(\cos\gamma, \sin\gamma, 0)$, respectively. In all the following calculations, E_F is computed at each angle with the constant electron number ($n_e = 3$), corresponding to the nondoped $Co_3Sn_2S_2$ [40,44].

First, we study the SHCs (AHC) for the changes in the magnetization angle α shown in Fig. 3(e). In Fig. 3(f), $\sigma_{yx}^{s_\mu}$ and $\sigma_{yx}^{\mathrm{AHE}}$ are computed as a function of α by considering only the Kane-Mele type SOC t_{KM}. When $\alpha = 90^\circ$, the magnetization is parallel to the applied electric field. Red, blue, green, and black lines indicate $\sigma_{yx}^{s_x}$, $\sigma_{yx}^{s_y}$, $\sigma_{yx}^{s_z}$, and $\sigma_{yx}^{\mathrm{AHE}}$, respectively. The sign of the AHC $\sigma_{yx}^{\mathrm{AHE}}$ (black line) changes when the magnetization flips [40]. One finds that when $\alpha = 0^\circ$ and $\alpha = 180^\circ$, $|\sigma_{yx}^{\mathrm{AHE}}| \sim |\sigma_{yx}^{s_z}|$ (green line) holds except for the unit $\hbar/2e$ because the spin Hall current is equal to the spin-polarized anomalous Hall current. $\sigma_{yx}^{s_x}$ (red line) can be finite and has a periodicity of 180°. On the other hand, $\sigma_{yx}^{s_y}$ (blue line) vanishes. In Fig. 3(g), the staggered Rashba SOC t_{sR} is considered in addition to t_{KM}. We note that $\sigma_{yx}^{\mathrm{AHE}}$ can be finite even without the out-of-plane component of the magnetization at $\alpha = 90^\circ$ and 270°. The

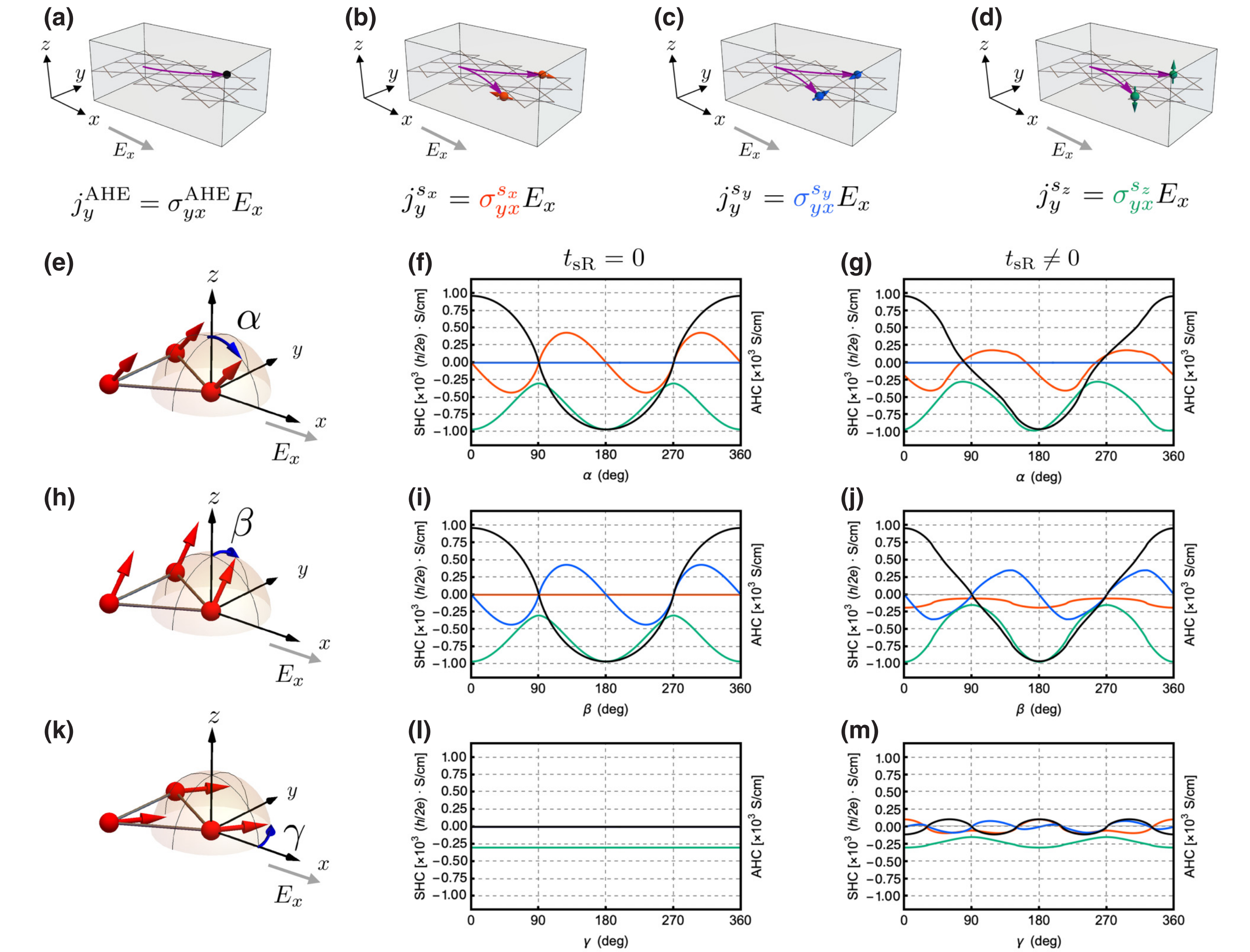

FIG. 3. Schematic figures of in-plane (a) anomalous Hall effect and (b)–(d) spin Hall effect induced by electric field E_x. (a) Anomalous Hall current flows in the y-direction and is characterized by the Hall conductivity $\sigma_{yx}^{\mathrm{AHE}}$. Spin Hall currents with spin angular momentum (b) s_x, (c) s_y, and (d) s_z flow in the y-direction and are characterized by the Hall conductivities $\sigma_{yx}^{s_x}$, $\sigma_{yx}^{s_y}$, and $\sigma_{yx}^{s_z}$, respectively. $\sigma_{yx}^{\mathrm{AHC}}$ (black), $\sigma_{yx}^{s_x}$ (red), $\sigma_{yx}^{s_y}$ (blue), and $\sigma_{yx}^{s_z}$ (green) (f) without and (g) with staggered Rashba SOC t_{sR}, as a function of tilting angle (e) α (in the x-z plane). (i),(j) The same for tilting angle (h) β (in the y-z plane). (l)(m) The same for tilting angle (k) γ (in the x-y plane).

periodicities of the Hall conductivities remain unchanged even with t_{sR}.

Next, we study the SHCs (AHC) for the changes in the magnetization angle β, as shown in Fig. 3(h). In Fig. 3(i), $\sigma_{yx}^{s_\mu}$ and $\sigma_{yx}^{\mathrm{AHE}}$ are computed as a function of β by considering only t_{KM}. When $\beta = 90^\circ$, the magnetization is parallel to the spin Hall current. The behaviors of $\sigma_{yx}^{\mathrm{AHE}}$ (black line) and $\sigma_{yx}^{s_z}$ (green line) are equivalent to those for the angle α [Fig. 3(f)]. We find that $\sigma_{yx}^{s_y}$ (blue line) can be finite, whereas $\sigma_{yx}^{s_x}$ (red line) vanishes. In Fig. 3(j), t_{sR} is considered in addition to t_{KM}. In contrast to the case with α, all the components of SHCs become finite. $\sigma_{yx}^{\mathrm{AHE}}$ (black line) vanishes at $\beta = 90^\circ$ and 270°, while $\sigma_{yx}^{\mathrm{AHE}}$ can be finite at $\alpha = 90^\circ$ and 270°.

Finally, we study the SHCs (AHC) for the changes in the magnetization angle γ shown in Fig. 3(k). When $\gamma = 0^\circ$, the magnetization is parallel to the applied electric field. As shown in Fig. 3(l), all the conductivities are independent of γ by considering only t_{KM}. We note that only $\sigma_{yx}^{s_z}$ (green line) is finite. In Fig. 3(m), t_{sR} is considered in addition to t_{KM}. All of the conductivities can be finite and show angular dependences.

V. OUT-OF-PLANE SPIN/ANOMALOUS HALL EFFECT

In the SOT experiment based on $Co_3Sn_2S_2$ mentioned previously [39,46], it is favorable to study the spin current flowing in the stacking (z) direction. Motivated by such

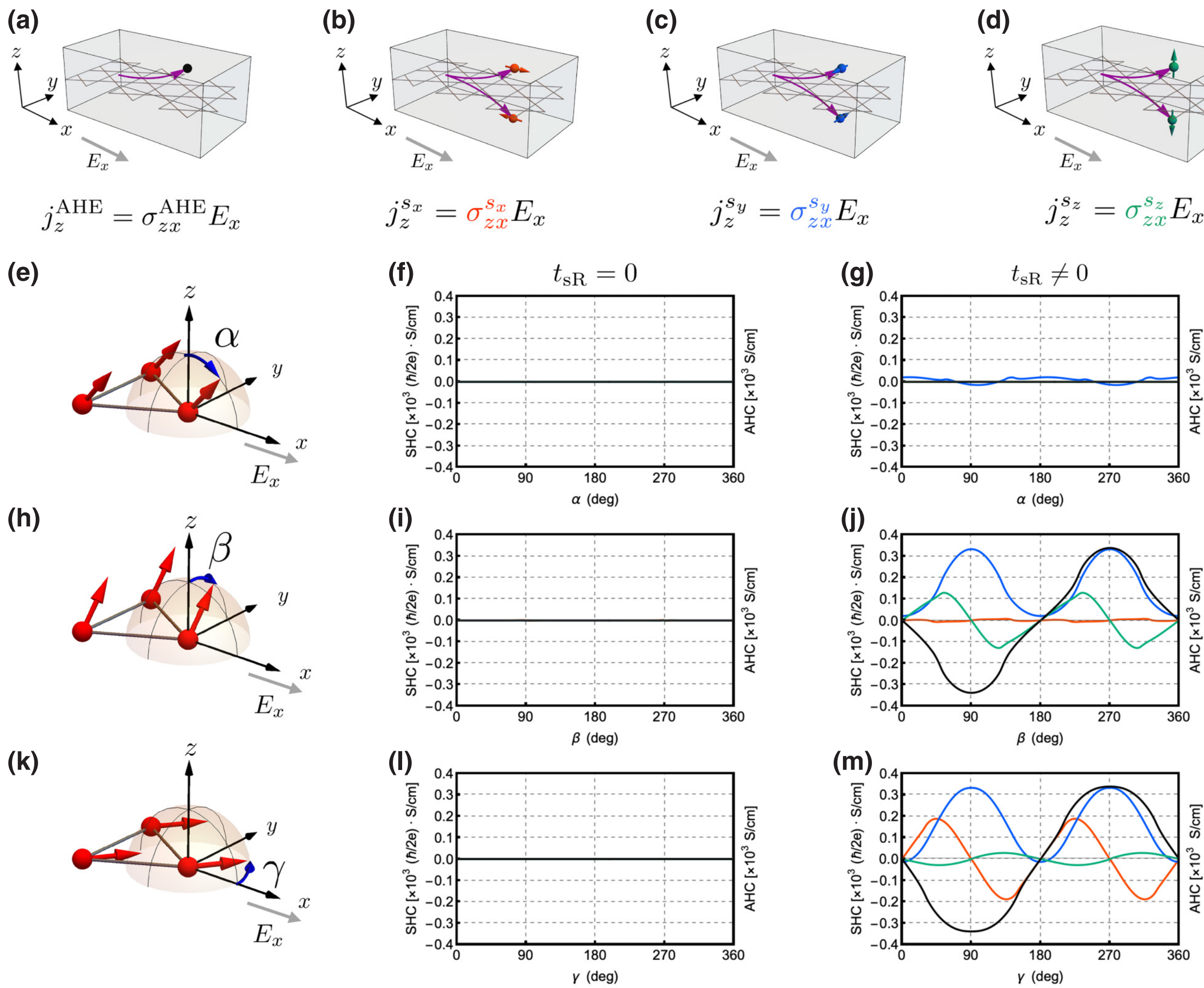

FIG. 4. Schematic figures of out-of plane (a) anomalous Hall effect and (b)–(d) spin Hall effect induced by applied electric field E_x. (a) Anomalous Hall current flows in the z-direction and is characterized by the Hall conductivity $\sigma_{zx}^{\mathrm{AHE}}$. Spin Hall currents with spin angular momentum (b) s_x, (c) s_y, and (d) s_z flow in the z-direction and are characterized by the spin Hall conductivities $\sigma_{zx}^{s_x}$, $\sigma_{zx}^{s_y}$, and $\sigma_{zx}^{s_z}$, respectively. $\sigma_{zx}^{\mathrm{AHC}}$ (black), $\sigma_{zx}^{s_x}$ (red), $\sigma_{zx}^{s_y}$ (blue), and $\sigma_{zx}^{s_z}$ (green) (f) without and (g) with staggered Rashba SOC t_{sR}, as a function of tilting angle (e) α (in the x-z plane). (i),(j) The same for different tilting angle (h) β (in the y-z plane). (l),(m) The same for different tilting angle (k) γ (in the x-y plane).

experiments, we study the out-of-plane SHE (AHE), where the spin (anomalous) Hall current $j_z^{s_\mu}$ (j_z^{AHE}) is induced by an electric field E_x, as shown in Figs. 4(a)–4(d). We find the characteristic angular dependences and enhancements of the Hall conductivities. The out-of-plane SHCs and AHC are denoted by $\sigma_{zx}^{s_\mu}$ and $\sigma_{zx}^{\mathrm{AHE}}$, respectively. We again consider the changes in the angles of the magnetization α, β, and γ [see Figs. 4(e), 4(h), and 4(k)]. Here, red, blue, green, and black lines indicate $\sigma_{zx}^{s_x}$, $\sigma_{zx}^{s_y}$, $\sigma_{zx}^{s_z}$, and $\sigma_{zx}^{\mathrm{AHE}}$, respectively. Figure 4 shows the out-of-plane Hall conductivities as a function of the angles as in Fig. 3. We notice that all the Hall conductivities vanish irrespective of the angles when only t_{KM} is finite [see Figs. 4(f), 4(i), and 4(l)]. Then we consider t_{sR} in addition to t_{KM}. In Fig. 4(g), for the angle α, $\sigma_{zx}^{s_y}$ (blue line) can be finite, and others vanish. In Figs. 4(j) and 4(m), for the angles β and γ, all of the Hall conductivities can be finite. $\sigma_{zx}^{s_y}$ (blue line) and $|\sigma_{zx}^{\mathrm{AHE}}|$ (black line) are maximized at $\beta = \gamma = 90^\circ$ and 270°. At those angles, we recall that the magnetization is perpendicular to the applied electric field and induced Hall currents. This enhancement of the out-of-plane AHC $\sigma_{zx}^{\mathrm{AHE}}$ is consistent with that obtained by first-principles calculations [36]. In Fig. 4(j), for the angle β, $\sigma_{zx}^{s_x}$ (red line) is negligible. On the other hand, in Fig. 4(m), for the angle γ, $\sigma_{zx}^{s_x}$ (red line) and $\sigma_{zx}^{s_y}$ (blue line) are comparable. In particular, for both angles β and γ, $|\sigma_{zx}^{s_z}|$ (green line) is enhanced around 60°, 120°, 240°, and 300° while it vanishes at 0°, 90°, 180°, and 270°. We emphasize that the distinct angular dependences of the Hall conductivities originate from the presence of the staggered Rashba type SOC.

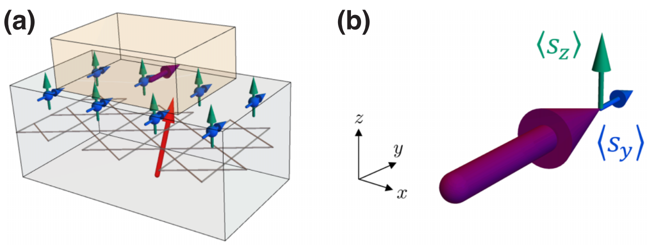

FIG. 5. (a) Possible configurations of spin accumulation $\langle s_y \rangle$ and $\langle s_z \rangle$ induced by out-of-plane spin Hall effect. (b) Relation between the in-plane magnetization and spin accumulations.

Before concluding this paper, we discuss the possibility of this system as a functional spin current generator. Here, we show that the SHE studied in this work might be useful for efficient magnetization switching. In the previous paragraph, we found the enhancement of the SHCs by tilting the magnetization. In particular, we showed the enhancement of $\sigma_{zx}^{s_y}$ (blue line) and $\sigma_{zx}^{s_z}$ (green line) as exhibited in Fig. 4(j). This implies that the y- and z-components of the spin accumulations ($\langle s_y \rangle$ and $\langle s_z \rangle$, respectively) are induced at the surface, as shown in Fig. 5(a). As mentioned previously, the recent experiment studied SOT in the devices of $Co_3Sn_2S_2$ attached to the in-plane magnetized CoFeB film [39]. Motivated by this experiment, we consider the same geometry where a ferromagnet is attached to the top of $Co_3Sn_2S_2$. In the attached ferromagnet, we assume that the macroscopic magnetization points in the y-direction, which is represented by a single purple arrow in Fig. 5(a). Additionally, when the ferromagnetic coupling exists near the interface, the magnetization of $Co_3Sn_2S_2$ (red arrow) may be tilted slightly even with the perpendicular magnetic anisotropy. This may yield an enhancement of the SHCs as mentioned previously. In this situation, let us discuss the SOT from $\langle s_z \rangle$ and $\langle s_y \rangle$ exerting on the magnetization, as shown in Fig. 5(b). First, we discuss two types of SOTs from $\sigma_{zx}^{s_z}$. The damping-like torque tends to align magnetization parallel to the z axis. The field-like torque drives the precession motion of the magnetization around the z axis. When the easy-plane magnetic anisotropy is present, the field-like SOT drives the precession motion of the magnetization in the easy plane, while the damping-like SOT generates the hard-axis component. We note that the flip of the electric field changes the direction of the field-like SOT. Nevertheless, the torque results in the precession motion of the magnetization. Turning to the SOTs from $\sigma_{zx}^{s_y}$, the damping-like torque can stabilize the magnetization pointing in the $+y$ axis. When the direction of the electric field is flipped, the antidamping-like torque points in the $-y$ direction, helping the switching of the magnetization. We note that the field-like torque, pointing in $+z$ or $-z$ direction, is ineffective when the easy plane magnetic anisotropy is present. In summary, a combination of the field-like torque from $\sigma_{zx}^{s_z}$ and the (anti)damping-like torque from $\sigma_{zx}^{s_z}$ may switch the magnetization efficiently, only with an electric field but without an external magnetic field.

VI. CONCLUSION

In this paper we theoretically studied the SHE in an effective model of magnetic Weyl semimetal $Co_3Sn_2S_2$. We showed the drastic changes of the SHCs depending on the direction of the magnetic moment. In particular, for the out-of-plane SHE, the enhancements of the SHCs were found. Our finding may help us design an efficient SOT generator for the in-plane magnetization switching based on the magnetic Weyl semimetal.

ACKNOWLEDGMENTS

The authors would like to thank Y. Araki, K. Fujiwara, Y. Kato, Y.-C. Lau, Y. Motome, K. Nakazawa, T. Seki, A. Tsukazaki, and Y. Yahagi for valuable discussions. This work was supported by JST CREST, Grant No. JPMJCR18T2 and by JSPS KAKENHI, Grant No. JP20H01830 and No. JP22K03446. A. O. was supported by GP-Spin at Tohoku University and by JST SPRING, Grant No. JPMJSP2114.

[1] M. Dyakonov and V. Perel, Current-induced spin orientation of electrons in semiconductors, Phys. Lett. A **35**, 459 (1971).
[2] Y. K. Kato, R. C. Myers, A. C. Gossard, and D. D. Awschalom, Observation of the spin Hall effect in semiconductors, Science **306**, 1910 (2004).
[3] J. Sinova, S. O. Valenzuela, J. Wunderlich, C. H. Back, and T. Jungwirth, Spin Hall effects, Rev. Mod. Phys. **87**, 1213 (2015).
[4] A. Chernyshov, M. Overby, X. Liu, J. K. Furdyna, Y. Lyanda-Geller, and L. P. Rokhinson, Evidence for reversible control of magnetization in a ferromagnetic material by means of spin–orbit magnetic field, Nat. Phys. **5**, 656 (2009).
[5] I. Mihai Miron, G. Gaudin, S. Auffret, B. Rodmacq, A. Schuhl, S. Pizzini, J. Vogel, and P. Gambardella, Current-driven spin torque induced by the Rashba effect in a ferromagnetic metal layer, Nat. Mater. **9**, 230 (2010).
[6] I. M. Miron, K. Garello, G. Gaudin, P.-J. Zermatten, M. V. Costache, S. Auffret, S. Bandiera, B. Rodmacq, A. Schuhl, and P. Gambardella, Perpendicular switching of a single ferromagnetic layer induced by in-plane current injection, Nature **476**, 189 (2011).
[7] L. Liu, O. J. Lee, T. J. Gudmundsen, D. C. Ralph, and R. A. Buhrman, Current-induced switching of perpendicularly magnetized magnetic layers using spin torque from the spin Hall effect, Phys. Rev. Lett. **109**, 096602 (2012).
[8] L. Liu, C.-F. Pai, Y. Li, H. Tseng, D. Ralph, and R. Buhrman, Spin-torque switching with the giant spin Hall effect of tantalum, Science **336**, 555 (2012).

[9] S. Fukami, T. Anekawa, C. Zhang, and H. Ohno, A spin–orbit torque switching scheme with collinear magnetic easy axis and current configuration, Nat. Nanotechnol. **11**, 621 (2016).
[10] G.-Y. Guo, S. Murakami, T.-W. Chen, and N. Nagaosa, Intrinsic spin Hall effect in platinum: First-principles calculations, Phys. Rev. Lett. **100**, 096401 (2008).
[11] B. F. Miao, S. Y. Huang, D. Qu, and C. L. Chien, Inverse spin Hall effect in a ferromagnetic metal, Phys. Rev. Lett. **111**, 066602 (2013).
[12] T. Taniguchi, J. Grollier, and M. D. Stiles, Spin-transfer torques generated by the anomalous Hall effect and anisotropic magnetoresistance, Phys. Rev. Appl. **3**, 044001 (2015).
[13] T. Seki, K.-I. Uchida, T. Kikkawa, Z. Qiu, E. Saitoh, and K. Takanashi, Observation of inverse spin Hall effect in ferromagnetic FePt alloys using spin Seebeck effect, Appl. Phys. Lett. **107**, 092401 (2015).
[14] M. Kimata, H. Chen, K. Kondou, S. Sugimoto, P. K. Muduli, M. Ikhlas, Y. Omori, T. Tomita, A. MacDonald, S. Nakatsuji, and Y. Otani, Magnetic and magnetic inverse spin Hall effects in a non-collinear antiferromagnet, Nature **565**, 627 (2019).
[15] X. R. Wang, Anomalous spin Hall and inverse spin Hall effects in magnetic systems, Commun. Phys. **4**, 55 (2021).
[16] V. T. N. Huyen, Y. Yanagi, and M.-T. Suzuki, Spin and anomalous Hall effects emerging from topological degeneracy in the Dirac fermion system CuMnAs, Phys. Rev. B **104**, 035110 (2021).
[17] O. Busch, B. Göbel, and I. Mertig, Spin Hall effect in noncollinear kagome antiferromagnets, Phys. Rev. B **104**, 184423 (2021).
[18] S. Hu, D.-F. Shao, H. Yang, C. Pan, Z. Fu, M. Tang, Y. Yang, W. Fan, S. Zhou, and E. Y. Tsymbal, *et al.*, Efficient perpendicular magnetization switching by a magnetic spin Hall effect in a noncollinear antiferromagnet, Nat. Commun. **13**, 1 (2022).
[19] T. Nan, C. X. Quintela, J. Irwin, G. Gurung, D.-F. Shao, J. Gibbons, N. Campbell, K. Song, S.-Y. Choi, and L. Guo, *et al.*, Controlling spin current polarization through non-collinear antiferromagnetism, Nat. Commun. **11**, 4671 (2020).
[20] K. Kondou, H. Chen, T. Tomita, M. Ikhlas, T. Higo, A. H. MacDonald, S. Nakatsuji, and Y. Otani, Giant field-like torque by the out-of-plane magnetic spin Hall effect in a topological antiferromagnet, Nat. Commun. **12**, 6491 (2021).
[21] Y. Araki, A. Yoshida, and K. Nomura, Universal charge and current on magnetic domain walls in Weyl semimetals, Phys. Rev. B **94**, 115312 (2016).
[22] K. Kuroda, T. Tomita, M.-T. Suzuki, C. Bareille, A. Nugroho, P. Goswami, M. Ochi, M. Ikhlas, M. Nakayama, and S. Akebi, *et al.*, Evidence for magnetic Weyl fermions in a correlated metal, Nat. Mater. **16**, 1090 (2017).
[23] Y. Araki, A. Yoshida, and K. Nomura, Localized charge in various configurations of magnetic domain wall in a Weyl semimetal, Phys. Rev. B **98**, 045302 (2018).
[24] A. Sakai, Y. P. Mizuta, A. A. Nugroho, R. Sihombing, T. Koretsune, M.-T. Suzuki, N. Takemori, R. Ishii, D. Nishio-Hamane, and R. Arita, *et al.*, Giant anomalous Nernst effect and quantum-critical scaling in a ferromagnetic semimetal, Nat. Phys. **14**, 1119 (2018).
[25] Q. L. He, T. L. Hughes, N. P. Armitage, Y. Tokura, and K. L. Wang, Topological spintronics and magnetoelectronics, Nat. Mater. **21**, 15 (2022).
[26] S. Maekawa, T. Kikkawa, H. Chudo, J. Ieda, and E. Saitoh, Spin and spin current—From fundamentals to recent progress, J. Appl. Phys. **133**, 020902 (2023).
[27] X. Wan, A. M. Turner, A. Vishwanath, and S. Y. Savrasov, Topological semimetal and Fermi-arc surface states in the electronic structure of pyrochlore iridates, Phys. Rev. B **83**, 205101 (2011).
[28] A. A. Burkov and L. Balents, Weyl semimetal in a topological insulator multilayer, Phys. Rev. Lett. **107**, 127205 (2011).
[29] E. Liu, *et al.*, Giant anomalous Hall effect in a ferromagnetic kagome-lattice semimetal, Nat. Phys. **14**, 1125 (2018).
[30] Q. Xu, E. Liu, W. Shi, L. Muechler, J. Gayles, C. Felser, and Y. Sun, Topological surface Fermi arcs in the magnetic Weyl semimetal $Co_3Sn_2S_2$, Phys. Rev. B **97**, 235416 (2018).
[31] Q. Wang, Y. Xu, R. Lou, Z. Liu, M. Li, Y. Huang, D. Shen, H. Weng, S. Wang, and H. Lei, Large intrinsic anomalous Hall effect in half-metallic ferromagnet $Co_3Sn_2S_2$ with magnetic Weyl fermions, Nat. Commun. **9**, 3681 (2018).
[32] D. Liu, A. Liang, E. Liu, Q. Xu, Y. Li, C. Chen, D. Pei, W. Shi, S. Mo, and P. Dudin, *et al.*, Magnetic Weyl semimetal phase in a Kagomé crystal, Science **365**, 1282 (2019).
[33] S. N. Guin, P. Vir, Y. Zhang, N. Kumar, S. J. Watzman, C. Fu, E. Liu, K. Manna, W. Schnelle, and J. Gooth, *et al.*, Zero-field Nernst effect in a ferromagnetic kagome-lattice Weyl-semimetal $Co_3Sn_2S_2$, Adv. Mater. **31**, 1806622 (2019).
[34] Y. Okamura, S. Minami, Y. Kato, Y. Fujishiro, Y. Kaneko, J. Ikeda, J. Muramoto, R. Kaneko, K. Ueda, and V. Kocsis, *et al.*, Giant magneto-optical responses in magnetic Weyl semimetal $Co_3Sn_2S_2$, Nat. Commun. **11**, 4619 (2020).
[35] L. Jiao, Q. Xu, Y. Cheon, Y. Sun, C. Felser, E. Liu, and S. Wirth, Signatures for half-metallicity and nontrivial surface states in the kagome lattice Weyl semimetal $Co_3Sn_2S_2$, Phys. Rev. B **99**, 245158 (2019).
[36] M. P. Ghimire, J. I. Facio, J.-S. You, L. Ye, J. G. Checkelsky, S. Fang, E. Kaxiras, M. Richter, and J. van den Brink, Creating Weyl nodes and controlling their energy by magnetization rotation, Phys. Rev. Res. **1**, 032044(R) (2019).
[37] Q. Zhang, S. Okamoto, G. D. Samolyuk, M. B. Stone, A. I. Kolesnikov, R. Xue, J. Yan, M. A. McGuire, D. Mandrus, and D. A. Tennant, Unusual exchange couplings and intermediate temperature Weyl state in $Co_3Sn_2S_2$, Phys. Rev. Lett. **127**, 117201 (2021).
[38] J. Watanabe, Y. Araki, K. Kobayashi, A. Ozawa, and K. Nomura, Magnetic orderings from spin–orbit coupled electrons on kagome lattice, J. Phys. Soc. Jpn. **91**, 083702 (2022).
[39] T. Seki, Y.-C. Lau, J. Ikeda, K. Fujiwara, A. Ozawa, S. Iihama, K. Nomura, and A. Tsukazaki, Enhancement of spin-charge conversion efficiency for $Co_3Sn_2S_2$ across

transition from paramagnetic to ferromagnetic phase, Phys. Rev. Res. **5**, 013222 (2023).

[40] A. Ozawa and K. Nomura, Two-orbital effective model for magnetic Weyl semimetal in kagome-lattice shandite, J. Phys. Soc. Jpn. **88**, 123703 (2019).

[41] C. L. Kane and E. J. Mele, Quantum spin Hall effect in graphene, Phys. Rev. Lett. **95**, 226801 (2005).

[42] H.-M. Guo and M. Franz, Topological insulator on the kagome lattice, Phys. Rev. B **80**, 113102 (2009).

[43] H. Chen, Q. Niu, and A. H. MacDonald, Anomalous Hall effect arising from noncollinear antiferromagnetism, Phys. Rev. Lett. **112**, 017205 (2014).

[44] A. Ozawa and K. Nomura, Self-consistent analysis of doping effect for magnetic ordering in stacked-kagome Weyl system, Phys. Rev. Mater. **6**, 024202 (2022).

[45] Y. Yanagi, J. Ikeda, K. Fujiwara, K. Nomura, A. Tsukazaki, and M.-T. Suzuki, First-principles investigation of magnetic and transport properties in hole-doped shandite compounds $Co_3In_xSn_{2-x}S_2$, Phys. Rev. B **103**, 205112 (2021).

[46] Y.-C. Lau, J. Ikeda, K. Fujiwara, A. Ozawa, J. Zheng, T. Seki, K. Nomura, L. Du, Q. Wu, A. Tsukazaki, and K. Takanashi, Intercorrelated anomalous Hall and spin Hall effect in kagome-lattice $Co_3Sn_2S_2$-based shandite films, Phys. Rev. B **108**, 064429 (2023).

[47] N. Nagaosa, J. Sinova, S. Onoda, A. H. MacDonald, and N. P. Ong, Anomalous Hall effect, Rev. Mod. Phys. **82**, 1539 (2010).

[48] W. Schnelle, A. Leithe-Jasper, H. Rosner, F. M. Schappacher, R. Pöttgen, F. Pielnhofer, and R. Weihrich, Ferromagnetic ordering and half-metallic state of $Sn_2Co_3S_2$ with the shandite-type structure, Phys. Rev. B **88**, 144404 (2013).